Check for updates

Geophysical Research Letters

RESEARCH LETTER
10.1029/2022GL101402

Key Points:

- We deduce the electron plasma density from Electric Field and Waves and Electric and Magnetic Field Instrument Suite and Integrated Science measurements (2012–2019) and extract the plasmasphere boundaries
- New plasmasphere boundary statistics and laws, binned by L, magnetic local time, and geomagnetic indices are generated to be used in space weather codes
- A density-based boundary is more frequently defined than is a gradient-based boundary, and yields a more frequently applicable model

Supporting Information:

Supporting Information may be found in the online version of this article.

Correspondence to:

J.-F. Ripoll,
jean-francois.ripoll@cea.fr

Citation:

Ripoll, J.-F., Thaller, S. A., Hartley, D. P., Cunningham, G. S., Pierrard, V., Kurth, W. S., et al. (2022). Statistics and empirical models of the plasmasphere boundaries from the Van Allen Probes for radiation belt physics. *Geophysical Research Letters*, *49*, e2022GL101402. https://doi.org/10.1029/2022GL101402

Received 22 SEP 2022
Accepted 19 OCT 2022

Author Contributions:

Conceptualization: J.-F. Ripoll, S. A. Thaller, D. P. Hartley, G. S. Cunningham, V. Pierrard, W. S. Kurth, C. A. Kletzing
Data curation: S. A. Thaller, D. P. Hartley, W. S. Kurth, C. A. Kletzing, J. R. Wygant
Formal analysis: J.-F. Ripoll, S. A. Thaller, D. P. Hartley, G. S. Cunningham
Funding acquisition: G. S. Cunningham, C. A. Kletzing
Investigation: J.-F. Ripoll, S. A. Thaller, D. P. Hartley, W. S. Kurth, C. A. Kletzing
Methodology: J.-F. Ripoll, S. A. Thaller, D. P. Hartley, G. S. Cunningham, V.

© 2022. American Geophysical Union. All Rights Reserved.

Statistics and Empirical Models of the Plasmasphere Boundaries From the Van Allen Probes for Radiation Belt Physics

J.-F. Ripoll[1,2], S. A. Thaller[3,4], D. P. Hartley[5], G. S. Cunningham[6], V. Pierrard[7,8], W. S. Kurth[5], C. A. Kletzing[5], and J. R. Wygant[9]

[1]CEA, DAM, DIF, Arpajon, France, [2]UPS, CEA, LMCE, Bruyères-le-Châtel, France, [3]Laboratory for Atmospheric and Space Physics, University of Colorado Boulder, Boulder, CO, USA, [4]Now at Orion Space Solutions, Louisville, CO, USA, [5]Department of Physics and Astronomy, University of Iowa, Iowa City, IA, USA, [6]Space Science and Applications Group, Los Alamos National Laboratory, Los Alamos, NM, USA, [7]Royal Belgian Institute for Space Aeronomy, STCE and Space Physics, Brussels, Belgium, [8]Université Catholique de Louvain (UCLouvain), Center for Space Radiations (CSR), Georges Lemaître Centre for Earth and Climate Research (TECLIM), Earth and Life Institute (ELI), Ottignies-Louvain-La-Neuve, Belgium, [9]School of Physics and Astronomy, University of Minnesota, Minneapolis, MN, USA

Abstract We deduce the electron plasma density from the NASA Van Allen Probes Electric Field and Waves and Electric and Magnetic Field Instrument Suite and Integrated Science measurements and extract the plasmasphere boundaries throughout 2012–2019. We use the gradient method for locating the plasmapause at L_{pp} and the 100 cm^{-3} density threshold for the plasmasphere outer edge at L_{100}. We show how, where, and when both L_{pp} and L_{100} coincide when the plasmapause gradient exists. L_{100} is demonstrated to bound the plasmasphere at large L-shell in the dusk. The plasmasphere expands farther out than predicted from the Carpenter and Anderson (1992, https://doi.org/10.1029/91JA01548) model. We generate statistics of the plasmasphere boundaries binned by L-shell, magnetic local time (MLT), and geomagnetic indices, leading to new models for radiation belt codes. The L_{100} boundary commonly varies by ~±0.5 L, increasing with activity up to ~±1 L, becomes MLT-dependent for Kp > ~2, and is preferentially steep on the night side for non-quiet times and a wider region in the afternoon sector.

Plain Language Summary The plasmasphere is a region of plasma extending out from the ionized upper part of the atmosphere to distances of 2–6 Earth Radii. The plasmasphere plasma is the coldest plasma (1/100–1/1,000,000 of the energy of other plasma) in the space around Earth where the particle motions are regulated by Earth's magnetic field (the magnetosphere). It is also high density, 100–10,000 times higher than elsewhere in the magnetosphere. The outer edge of the plasmasphere, called the plasmapause, typically drops from >100 to <10 cm^{-3} over a relatively short distance. Waves that energize radiation belt particles (chorus) are found outside the plasmasphere. Inside the plasmasphere are different waves (hiss) that cause radiation belt particles to precipitate into Earth's atmosphere. Therefore, models predicting the radiation belt's behavior need to know the plasmapause location. To predict the plasmapause position, we analyze 7 years of Van Allen Probes data to find the plasma density in two different ways, using both the 100 cm^{-3} density and the density gradient. We look at how their locations change with the level of geomagnetic storm activity and deduce new plasmasphere boundaries models for space weather codes.

1. Introduction

The Earth's plasmapause was originally defined as a "knee," that is, "an abrupt decrease in density," separating the dense plasmasphere (>~100 cm^{-3}) from the low density plasmatrough region (>~1 cm^{-3}) (Carpenter, 1966). It can be as close to Earth as $L < 2$ during the most intense storms and extend to $L > 6$ at equatorial latitudes during prolonged periods of low geomagnetic activity (e.g., Carpenter & Anderson, 1992; J. Tu et al., 2007). Plasmaspheric plasma has been found up to $L = 9$ at high latitude (33°) on the dawn side (Denton et al., 2004). During active times, a steep density gradient clearly defines the plasmapause. During quiet times, the plasmapause can have a significant width, with density varying between ~100 and ~10 cm^{-3}, and with a gradient that does not fulfill the traditional definition. This makes defining a plasmapause density value within these bounds somewhat arbitrary (Carpenter & Anderson, 1992; Carpenter & Lemaire, 2004; Goldstein, Sandel, et al., 2003).

19448007, 2022, 21, Downloaded from https://agupubs.onlinelibrary.wiley.com/doi/10.1029/2022GL101402 by EVIDENCE AID - BELGIUM, Wiley Online Library on [05/11/2022]. See the Terms and Conditions (https://onlinelibrary.wiley.com/terms-and-conditions) on Wiley Online Library for rules of use; OA articles are governed by the applicable Creative Commons License

Pierrard, W. S. Kurth, C. A. Kletzing, J. R. Wygant
Project Administration: J.-F. Ripoll
Resources: S. A. Thaller, D. P. Hartley
Software: J.-F. Ripoll, S. A. Thaller, D. P. Hartley, C. A. Kletzing
Supervision: J.-F. Ripoll
Validation: J.-F. Ripoll, S. A. Thaller, D. P. Hartley, W. S. Kurth, C. A. Kletzing
Visualization: J.-F. Ripoll, S. A. Thaller, D. P. Hartley
Writing – original draft: J.-F. Ripoll
Writing – review & editing: J.-F. Ripoll, S. A. Thaller, D. P. Hartley, G. S. Cunningham, V. Pierrard, W. S. Kurth

In this letter, we seek the Earth's plasmasphere boundaries in L using two methods; either as a gradient, L_{pp}, when it exists, or as a dense outer edge of the plasmasphere close to the 100 cm^{-3} density level, L_{100}. Comparing the position of L_{pp} and L_{100} when both exist allows us to conclude that both boundaries converge toward the plasmapause location with some newly quantified accuracy.

For Earth's radiation belt codes, the electron density (appearing in the index of refraction and the plasma frequency, see Equations 2, 3, 6, 7, 9, and 10 of Albert, 2005) matters for parameterizing the diffusion coefficient rather than the density gradient. But when statistical wave models are used as parameters in the diffusion coefficients, a common practice (e.g., Glauert et al., 2018; Ripoll, Claudepierre, et al. (2020)) is to specify a location in L to delineate between the high-density region where plasmaspheric hiss waves are present and the low-density region where chorus waves occur, with each wave causing different local loss and acceleration processes by wave-particle interactions (Thorne, 2010).

New hiss wave models are directly defined from the Earth's plasmapause position (Malaspina et al., 2016). Hiss power is correlated with density and monotonically increases with increasing density (Malaspina et al., 2018). Their Figure 2 shows the hiss power is minimal below ∼50–100 cm^{-3}, a limit defining the density threshold we track here. Chorus wave power does not correlate similarly with density, but the majority of the wave power occurs in the diluted region (∼1–10 cm^{-3}) (Malaspina et al., 2021). The outer edge of the plasmasphere, inside which hiss exists, becomes the relevant spatial marker for radiation belt simulations (Ripoll, Denton, Loridan, et al., 2020). An extended plasmasphere can contain significant hiss wave power causing the Earth's outer radiation belt decay (Pierrard, Ripoll, et al., 2021; Ripoll et al., 2016, 2019; Zhao et al., 2019), but does not often exhibit a well-defined plasmapause gradient. In these cases, replacing an absent gradient by a reliable alternative (here, L_{100}) becomes critical. Here, the density threshold value is specifically chosen for separating hiss and chorus in radiation belt codes and may not be optimal for other applications (or planets).

There exist a variety of terrestrial plasmapause models which can be used in radiation belt simulations. W. Tu et al. (2009) used the CRRES data driven model of O'Brien and Moldwin (2003). O'Brien and Moldwin (2003) also showed the relevance of parametrizing the plasmapause model with various indices such as Kp, AE, and Dst, as followed here. Other plasmapause models include Moldwin et al. (2002) and Bandić et al. (2016) based on CRRES data, Cho et al. (2015), Liu and Liu (2014), and Liu et al. (2015) based on THEMIS data, Larsen et al. (2007) based on IMAGE data, Verbanac et al. (2015) based on CLUSTER data and He et al. (2017) from multiple sources. A comparison of these models is provided in Pierrard, Botek, et al. (2021) and Guo et al. (2021). The Carpenter and Anderson (1992) plasmapause model (noted CA92) has been largely used for radiation belt studies over the last 10 years (e.g., Cervantes, Shprits, Aseev, & Allison, 2020; Cervantes, Shprits, Aseev, Drozdov, et al., 2020; Glauert et al., 2014; Kim et al., 2011; Malaspina et al., 2020; Ripoll et al., 2016; Saikin et al., 2021; Shprits et al., 2013; Subbotin & Shprits, 2009; W. Tu et al., 2013; Wang & Shprits, 2019). Physics-based models also provide plasma density and plasmapause location (e.g., Pierrard, Botek, and Darrouzet (2021)), with some models integrating Van Allen Probes measurements (e.g., Botek et al., 2021). Goldstein et al. (2019) generated a plasmapause statistical model from the simulations of 60 storms, which this study can help validate. Missing the plasmapause location misplaces local acceleration from chorus waves in simulations (Reidy et al., 2021).

In Section 2, we present the plasma density measured by the NASA Van Allen Probes (Mauk et al., 2013) during the entire mission. We compare the threshold and gradient methods and derive new statistics from them (Section 3). Plasmapause models with different parametrizations with respect to magnetic local time (MLT) and geomagnetic indices are given in Section 4 and and the Kp-dependent model is compared with both data and the CA92 model in Section 5. Conclusions are summarized in Section 6.

2. Electron Density and Plasmasphere Boundaries

2.1. The Electron Density Measured by the Van Allen Probes

The Van Allen Probes cold plasma densities can be determined using the spacecraft floating potential (Thaller et al., 2015) measured by the Electric Field and Waves (EFW) instrument (Wygant et al., 2013) and based on the functional relationship between the ambient plasma density and the spacecraft potential (Escoubet et al., 1997; Torkar et al., 2016, 2019). In this method, the densities used to perform the fit are extracted from the Electric and Magnetic Field Instrument Suite and Integrated Science (EMFISIS) Waves instrument (Kletzing et al., 2013) upper hybrid frequency, f_{UHR}, (Kurth et al., 2015). EFW densities are generated for the whole Van Allen Probe

19448007, 2022, 21, Downloaded from https://agupubs.onlinelibrary.wiley.com/doi/10.1029/2022GL101402 by EVIDENCE AID - BELGIUM, Wiley Online Library on [05/11/2022]. See the Terms and Conditions (https://onlinelibrary.wiley.com/terms-and-conditions) on Wiley Online Library for rules of use; OA articles are governed by the applicable Creative Commons License

B mission, from 26 December 2012 to 16 July 2019 (referred as EFW data). In addition, f_{UHR} densities derived from Van Allen Probes B EMFISIS data from 27 August 2012 to 16 July 2019 (referred as EMFISIS data) are also used.

All measured densities are linearly averaged into 0.1 L bins for each half orbit. The binning corresponds to a fine L-shell resolution for radiation belt studies (e.g., Li et al., 2014; Ripoll et al., 2017) and averages finer scale density structures. There are on average 20 ± 22 data points per 0.1 L ($L < 6.6$, EFW densities). Figure 1a shows the EFW density plotted for the whole Van Allen Probe B mission. The L-shell L refers here to the dipole L. Erosion of the plasmasphere is commonly visible down to $L \sim 3$ during storms. Plasmaspheric densities of 100 cm^{-3} can extend beyond L of 6 during quiet times (Figure 1b). The transition region between 10 and 100 cm^{-3} can exceed ∼1 L. Figures 1c and 1d show the mean plasma density in (L, MLT) polar plots sorted by geomagnetic activity as described by the Dst index. The plasmasphere appears azimuthally symmetric for Dst > −5. As Dst decreases to Dst < −15, an asymmetry forms in the morning (00–06 MLT) and afternoon sectors (12–18 MLT). The outward expansion of the plasma density in the afternoon sector (13–16 MLT) during active times is remarkable, particularly apparent in the 100 cm^{-3} line for Dst in (−60, −90). The mean density also increases in some of the night/morning sectors due to detached plasma regions rolling and wrapping around Earth. For very intense events, MLT resolution is lacking (cf. number of data points inserted in Figures 1c–1j).

2.2. Method of Determining Plasmasphere Boundaries

2.2.1. The Plasmapause

The plasmapause, L_{pp}, is determined using the original density gradient method from CA92, defined as a variation of the density by a factor 5 within half L for each half-orbit. This method is the most common (e.g., Moldwin et al. (2002), Malaspina et al. (2016)) and is here applied to 0.1 L binned EFW and EMFISIS densities. For each half-orbit, we always retain the first encountered gradient and record the inner L value.

2.2.2. The Dense Outer Edge of the Plasmasphere

The dense outer edge of the plasmasphere, L_{100}, is defined by the L value at a density threshold of ∼100 cm^{-3} following Carpenter (1966). For each half orbit, we search for the first minimum of the density below the 100 cm^{-3} threshold and in the (30, 100) range using the 0.1 L binned data. This ensures to exclude other maxima (>100 cm^{-3}) at higher L-shells. This avoids locating the plasmapause in detached dense regions but can locate the inner edge of wide inner cavities (Carpenter et al., 2000; Goldstein, Spasojević, et al., 2003), though the 0.1 L binning helps in removing fine scale structures. (Detached plasmas or plumes have to be treated separately from the main plasmasphere as they often contain intense hiss waves (e.g., Millan et al., 2021)). Among the 14,907 L_{100} values in Figure 1b, 42% falls ideally in the (30–100) range. A problem arises when the density abruptly drops from a few hundreds of cm^{-3} to below 30 cm^{-3}. In that case, we search for any timestamps at which the density was undefined between these values (e.g., small gaps in density). Such gaps occur if neither the EFW or EMFISIS technique are able to determine density values. If all timestamps have an associated density value (no gaps), we retain the location of the closest density that is greater than 100 cm^{-3} as L_{100}. For instance, if the density drops from 300 cm^{-3} at L_{i-1} to 20 cm^{-3} at L_i, the algorithm retains $L_{100} = L_{i-1}$ with $ne_{100} = 300$ cm^{-3}. Otherwise, if some (or all) densities at lower L-shells are undefined, the plasmapause is marked as undetermined (16% of all cases). The same method is applied to EMFISIS data. Verification of the method is available in Ripoll, Denton, Loridan et al. (2020) for March 2013, with further verification against EMFISIS data presented below.

Comparisons of L_{100} values from both methods/instruments confirm their good agreement (Figures 1k and 1l), with the bulk of normalized differences below ±20%. This is in agreement with Jahn et al. (2020), who found the ratio of EMFISIS and EFW densities fall within a range 0.5–2, with the majority of these ratios around 1, for example, $n_{EFW} \sim n_{EMFISIS}$ (in the range ∼10 to 3,000 cm^{-3}). The L_{100} boundary is dynamic, often varying by 0.5 L from one half orbit to another. During the Van Allen Probes era, the minimum L_{100} is generally $2.5 < L_{100} < 3$, during the 1 March 2015 storm for example, (e.g., Ozeke et al., 2019; Pierrard & Rosson, 2016). We see long-term variations with the plasmasphere expanding progressively from $L = 3$ to $L = 6$ during periods of ∼10 days or more. Plasmaspheric recovery from $L = 3$ to $L = 5$ can be fast for some events, taking about ∼3 days based on inspection of the time series data. Computing the boundary from the 50 cm^{-3} threshold (instead of 100 cm^{-3}) shows only minor differences, indicating that the method is not too sensitive to the threshold value, in accordance with Malaspina et al. (2016).

19448007, 2022, 21, Downloaded from https://agupubs.onlinelibrary.wiley.com/doi/10.1029/2022GL101402 by EVIDENCE AID - BELGIUM, Wiley Online Library on [05/11/2022]. See the Terms and Conditions (https://onlinelibrary.wiley.com/terms-and-conditions) on Wiley Online Library for rules of use; OA articles are governed by the applicable Creative Commons License

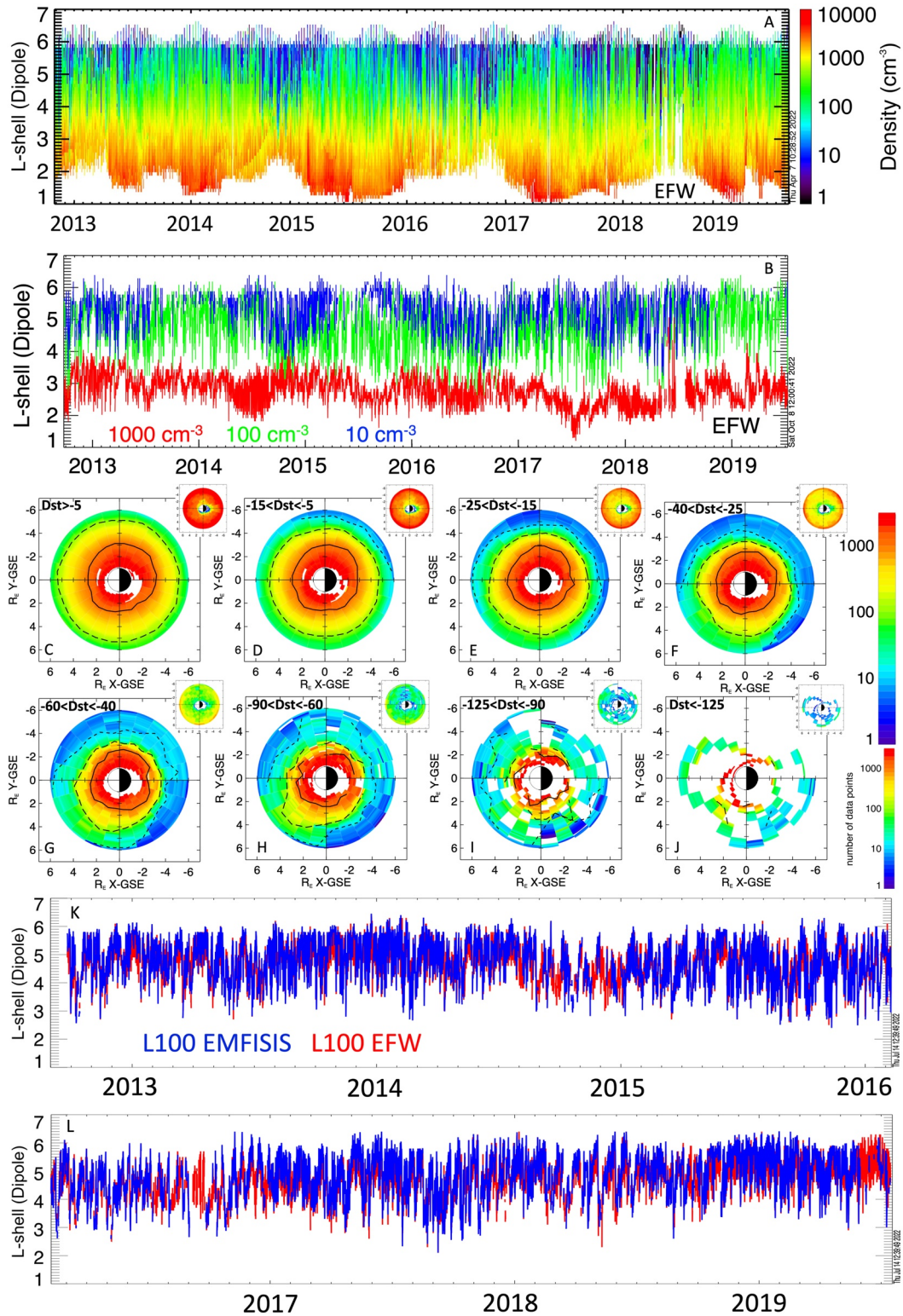

Figure 1. (a) The Electric Field and Waves (EFW) electron plasma density ($\log_{10}$ in cm^{-3}) from Van Allen Probes B during the whole mission with (b) 3 level lines extracted. (c–j) The mean density in (L and magnetic local time) and (small insert) data point number for 8 bins of Dst with level lines of (solid) 1,000 cm^{-3}, (long dashed) 100 cm^{-3}, (dashed) 10 cm^{-3}. (k, l) L_{100} for Electric and Magnetic Field Instrument Suite and Integrated Science (blue) and EFW (red).

19448007, 2022, 21, Downloaded from https://agupubs.onlinelibrary.wiley.com/doi/10.1029/2022GL101402 by EVIDENCE AID - BELGIUM, Wiley Online Library on [05/11/2022]. See the Terms and Conditions (https://onlinelibrary.wiley.com/terms-and-conditions) on Wiley Online Library for rules of use; OA articles are governed by the applicable Creative Commons License

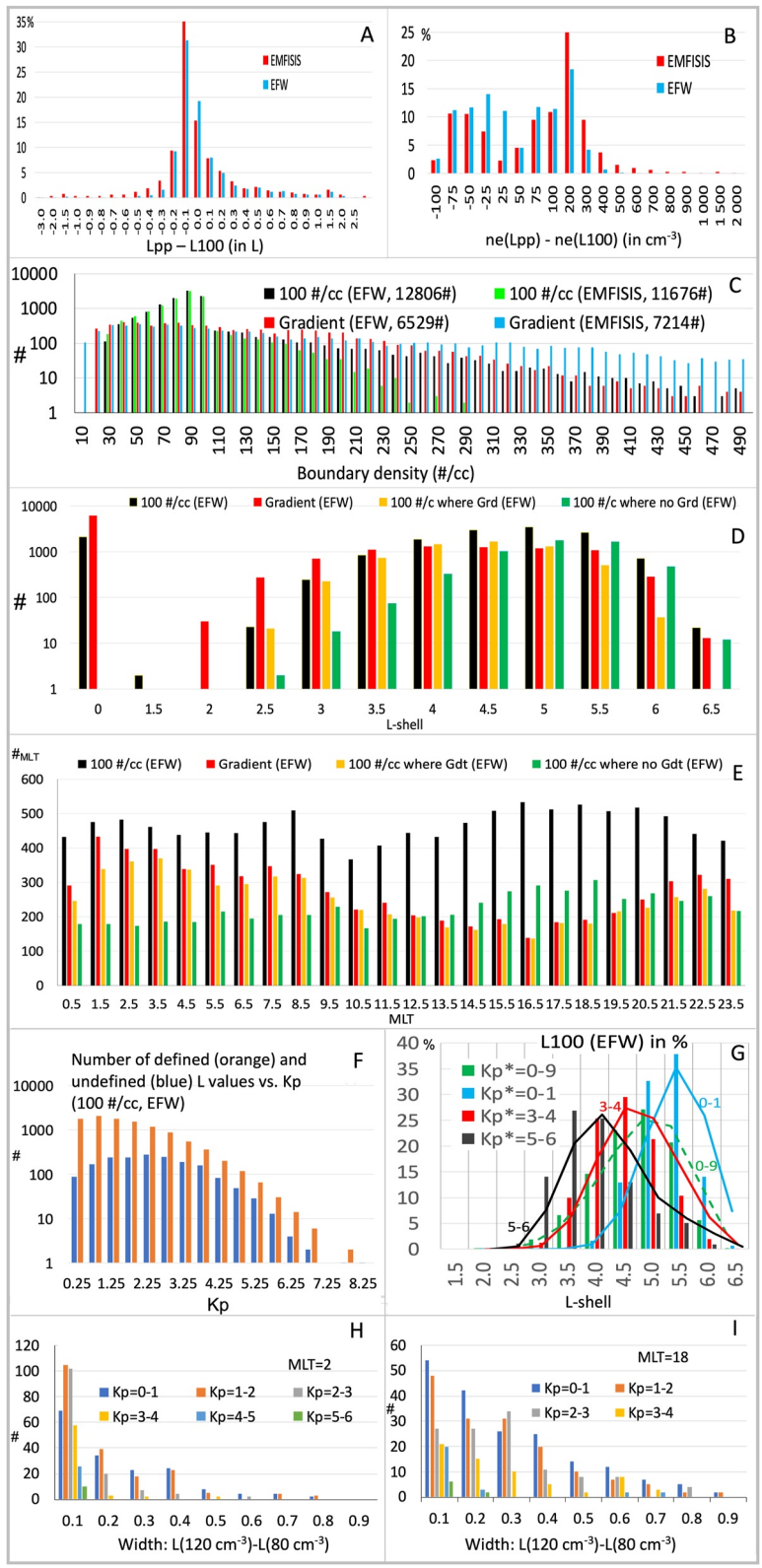

Figure 2. Probability of the difference between the threshold (L_{100}) and gradient (L_{pp}) methods given in (a) L value and (b) density. Distributions of the (c) density, (d) L value, and (e) magnetic local time (MLT) (in #) at the 100 cm^{-3} (L_{100}) and gradient (L_{pp}) positions (Electric Field and Waves [EFW] data). Undetermined L value plotted at $L = 0$ in panel (d). Distributions of (orange) defined and (blue) undefined L_{100} values, sorted by (f) Kp index (EFW data). (g) Distributions of L_{100} (in % of data) versus L-shell and Kp*. Distribution of the boundary width (h) on the night side (MLT = 2) and (i) on the day side (MLT = 18) for Kp bins (EFW data).

19448007, 2022, 21, Downloaded from https://agupubs.onlinelibrary.wiley.com/doi/10.1029/2022GL101402 by EVIDENCE AID - BELGIUM, Wiley Online Library on [05/11/2022]. See the Terms and Conditions (https://onlinelibrary.wiley.com/terms-and-conditions) on Wiley Online Library for rules of use; OA articles are governed by the applicable Creative Commons License

3. Statistics of the Plasmasphere Boundaries

3.1. Direct Comparison of Threshold and Gradient Methods

Figure 2a shows a direct comparison between the threshold, L_{100}, and gradient, L_{pp}, methods for each half-orbit when both are defined; 53% of differences ($L_{pp} - L_{100}$) are within [−0.1 L, 0.1 L], 69% within [−0.2 L, 0.2 L], 77% within [−0.3 L, 0.3 L], and 86% within [−0.5 L, 0.5 L]. The density difference ($n_{pp} - n_{100}$) at L_{100} and L_{pp} is ±100 cm^{-3} for 75% of cases and in (−100, 300) cm^{-3} for 97% of cases (Figure 2b). A normalized density difference, $100(L_{pp} - L_{100})/L_{pp}$, of (±50%, ±100%, ±200%) represents (37%, 82%, 93%) of cases. Some differences are due to the gradient not existing (e.g., quiet times, dayside) or the existence of a boundary width (Section 3.3). These results confirm the "knee" is often close to ∼100 cm^{-3} (Carpenter, 1966), supporting a labeling of the outer edge of the plasmasphere at ∼100 cm^{-3} as the plasmapause (when a gradient exits), and show its computation is possible with a threshold method. Reasons for using a threshold method are simplicity, the dense outer edge is more often defined (see below), the threshold value delineates plasmaspheric waves from chorus waves, and the method is consistent with radiation belt codes not requiring a density gradient.

3.2. Statistics of L_{100} and L_{pp}

Figure 2c shows the distribution of the density values n_{pp} and n_{100} corresponding respectively to L_{pp} and L_{100} from EFW and EMFISIS data. In Figure 2c, we compute n_{pp} is lower than (10, 30, 100, 200, 400) cm^{-3} for (5%, 15%, 52%, 86%, 94%) of the cases (EFW data). The mean(median) n_{100} value is n_e = 98(89) cm^{-3}. Most (83%) of n_{100} values are between 30 and 100 cm^{-3} (EFW data), 16.7% between 100 and 490 cm^{-3}, and 0.23% above 490 cm^{-3} (not plotted). These $n_{100} > 490$ cm^{-3} values correspond to sharp gradients or abrupt erosions occurring inside the dense plasmasphere during storms, which are well captured by the threshold method. This explains that n_{100} can be at much higher density than 100 cm^{-3} (as can L_{pp} and therefore n_{pp}), thus explaining why the threshold method can work. We conclude the 100 cm^{-3} level falls in great majority within the gradient width (when it exists), becoming a reliable statistical marker of the plasmapause location.

Figure 2d presents the sample distributions of the boundary locations. The L_{pp} is defined for only 53% of the half orbits (undefined values plotted at $L = 0$), demonstrating the need for a reliable alternative. Conversely, L_{100} is defined in 85% of cases, highlighting that it can fulfill this need. A L_{100} value below $L = 3$ represents 2% of the cases (only three events fall below $L = 2 \pm 0.25$). Ninety-five percents are between $3.25 < L < 5.75$ and 50% identifications occur between $4.25 < L < 5.25$, with a quite flat distribution. L_{100} data reaches 5.5 ± 0.25 commonly in 18% of cases and up to $L = 6 \pm 0.25$ in 5% of cases, associated with quiet times, which confirms the influence of the plasmasphere (through the hiss power contained in it) far inside the outer radiation belt (e.g., Ripoll et al., 2019; Ripoll, Denton, Hartley, et al., 2020).

Figure 2e provides MLT distributions. The gradient method finds apparently more plasmapause crossings where erosion is strongest (night/dawn) and less where extended or diluted plasmasphere occurs due to expansion and plume dynamics (noon/dusk), which confirms a bias of the gradient method in favor of the night/dawn side. Statistics, which are limited to data for which both L_{pp} and L_{100} are defined, show similar behavior in L-shell and MLT (Figures 2d and 2e). On the contrary, statistics restricted to data for which L_{100} is defined but L_{pp} is not defined show the threshold method offers a boundary peaked at rather high L-shell and on the dusk side. Figures 2d and 2e generated from EMFISIS data show similar behaviors (see Figures S1 and S2 in Supporting Information S1). Therefore, the 100 cm^{-3} outer edge of the plasmasphere encompasses (or approximates) the plasmapause when it exists, provides an L-shell limit in the dusk for the diluted plasmasphere, and avoids the statistical bias on the night/dawn side of the gradient method.

3.3. Distributions With Respect to Geomagnetic Conditions

Figure 2f and Figure S3 in Supporting Information S1 show the number of L_{100} locations for a given geomagnetic index (EFW data). Undetermined L_{100} locations are also shown (blue). For bins where Dst > −55, AE < 750, and Kp < 5.5 we have over 100 L values, indicating that statistics are adequate. Bins with below 10 cases are considered under resolved, namely Kp > 6.5, Dst < −110, and AE > 1,100. Figure 2g shows how the distributions of L_{100} reaches lower L-shells as Kp* increases, with always a large spread over L-shell of ∼2 L for a given Kp* bin (see full distribution in Figure S4 in Supporting Information S1).

19448007, 2022, 21, Downloaded from https://agupubs.onlinelibrary.wiley.com/doi/10.1029/2022GL101402 by EVIDENCE AID - BELGIUM, Wiley Online Library on [05/11/2022]. See the Terms and Conditions (https://onlinelibrary.wiley.com/terms-and-conditions) on Wiley Online Library for rules of use; OA articles are governed by the applicable Creative Commons License

19448007, 2022, 21, Downloaded from https://agupubs.onlinelibrary.wiley.com/doi/10.1029/2022GL101402 by EVIDENCE AID - BELGIUM, Wiley Online Library on [05/11/2022]. See the Terms and Conditions (https://onlinelibrary.wiley.com/terms-and-conditions) on Wiley Online Library for rules of use; OA articles are governed by the applicable Creative Commons License

3.4. Width of the Plasmasphere Outer Edge

We compute the L-shell variation between 120 and 80 cm^{-3}, defining a boundary width, $W = L(n_e = 120\ cm^{-3}) - L(n_e = 80\ cm^{-3})$ (EFW data), with results shown in Figures 2k and 2l. We find either a minimal width ($W \sim 0.1$ L) indicative of sharp gradients, or a diluted boundary layer (of various width) depending on MLT. Sharp gradients occur predominantly on the night side and during active times (shown at MLT = 2 in Figure 2l). As activity increases, the compression of the magnetosphere closes the magnetospheric flow closer to the Earth on the night side, which sharply cuts off the outer plasmasphere. The distribution is very different on the dayside in the afternoon sector (shown at MLT = 18 in Figure 2k), often wider, with a distribution spread over various widths for any Kp index. This is due to the diluted expansion of the plasmasphere at large L-shell for low Kp as well as to ionospheric outflows, sunward expulsion of plasmaspheric electrons, and plume formation at higher Kp index (e.g., Borovsky & Denton, 2008; Krall et al., 2018).

4. New Plasmasphere Boundary Models for Earth's Radiation Belt Physics

We present in Figure 3 new empirical models of the mean and standard deviation of the 100 cm^{-3} outer edge of the plasmasphere, L_{100}, according to geomagnetic indices, with MLT dependence (right) and without (left) (EFW data). Mean and standard deviation allow for uncertainty quantification of radiation belt simulation (Camporeale et al., 2016).

Figure 3 (center, left) also shows further comparison of the EFW and the EMFISIS L_{100} value (red line) for various Kp. The agreement between both is excellent with a difference by 0.1–0.2 L for Kp < 4. The largest difference can reach 0.3 L for some Kp bins, such as for Kp = 5 and Kp = 6.5, within the standard deviation.

The standard deviation is $\sim\pm$0.5 L and minimal for quiet times (defined here by Kp < 2, AE < 300, and Dst > −50). The standard deviation increases with geomagnetic activity, up to $\sim\pm$1 L. There is a large variability with geomagnetic activity, also indicating the complexity in describing the plasmasphere boundary with a single index.

Figure 3 (right column) shows MLT-dependent statistical laws with respect to each starred geomagnetic index (defined as the maximum for Kp and AE and the minimum for Dst over the previous 24 hr). Using starred indices shifts the distribution toward higher Kp or AE or more negative Dst (dots in Figure 3). The mean and median L values versus Dst* are very close to each other so that only the mean is provided. L_{100} becomes MLT-dependent for Dst* < −20, AE* > 600, and Kp* > 3, which justifies keeping the MLT dependence in the new models. Comparing with Figure 1, this occurs for higher activity due to the use of Dst* instead of Dst. The strong asymmetry due to plume dynamics during strong storms is apparent for Dst* < −100, AE* > 1,200, and Kp* > 6. Data and fits for Dst* < −120, AE* > 1,400, and Kp* > 6.5 are statistically under-resolved.

A linear dependence $L_{100/pp} = b - a\mathrm{Kp}^*$ is apparent in Figure 3 (center), in agreement with O'Brien and Moldwin (2003). We find a = (0.36/0.38/0.31/0.25/0.34) and b = (5.62/5.57/5.59/5.48/5.51) for L_{100} and a = (0.34/0.41/0.34/0.21/0.38) and b = (5.63/5.62/5.48/5.27/5.47) for L_{pp} (gradient method) at centered MLT = (00/06/12/18/All) for Kp* ≤ 6 (EFW data). Using EMFISIS data and the gradient method for all MLT, we recover the fit of the CA92 model, itself generated from density gradients observed with ISEE (range 0–15 MLT): L_{pp} = 5.60–0.46 Kp*. This may be fortuitous as the CA92 MLT range is partial but seemingly demonstrates the practical reliability of this L_{pp} model.

For AE and Dst indices, we recommend directly using the mean and standard deviation values of Figure 3 (available in Thaller and Ripoll (2022)). These MLT-dependent laws can be directly used in current radiation belt codes in order to better account for the plasmasphere asymmetry and more accurately separate hiss from chorus.

5. Comparison of Empirical Models With Observations

We compare both the Kp* MLT-dependent L_{100} model described above and the L_{pp} from CA92 with the L_{100} EFW observations (Figures 4a and 4b), providing their respective normalized difference, $\mathrm{ND} = (L_{100} - L_{\mathrm{modelorCA92}})/L_{100}$ (Figures 4c and 4d). This is shown for years 2012–2016 (see Figure S5 in Supporting Information S1 for 2016–2019). A slight upwards shift is visible, along with more fluctuations, for the CA92 model. The distribution

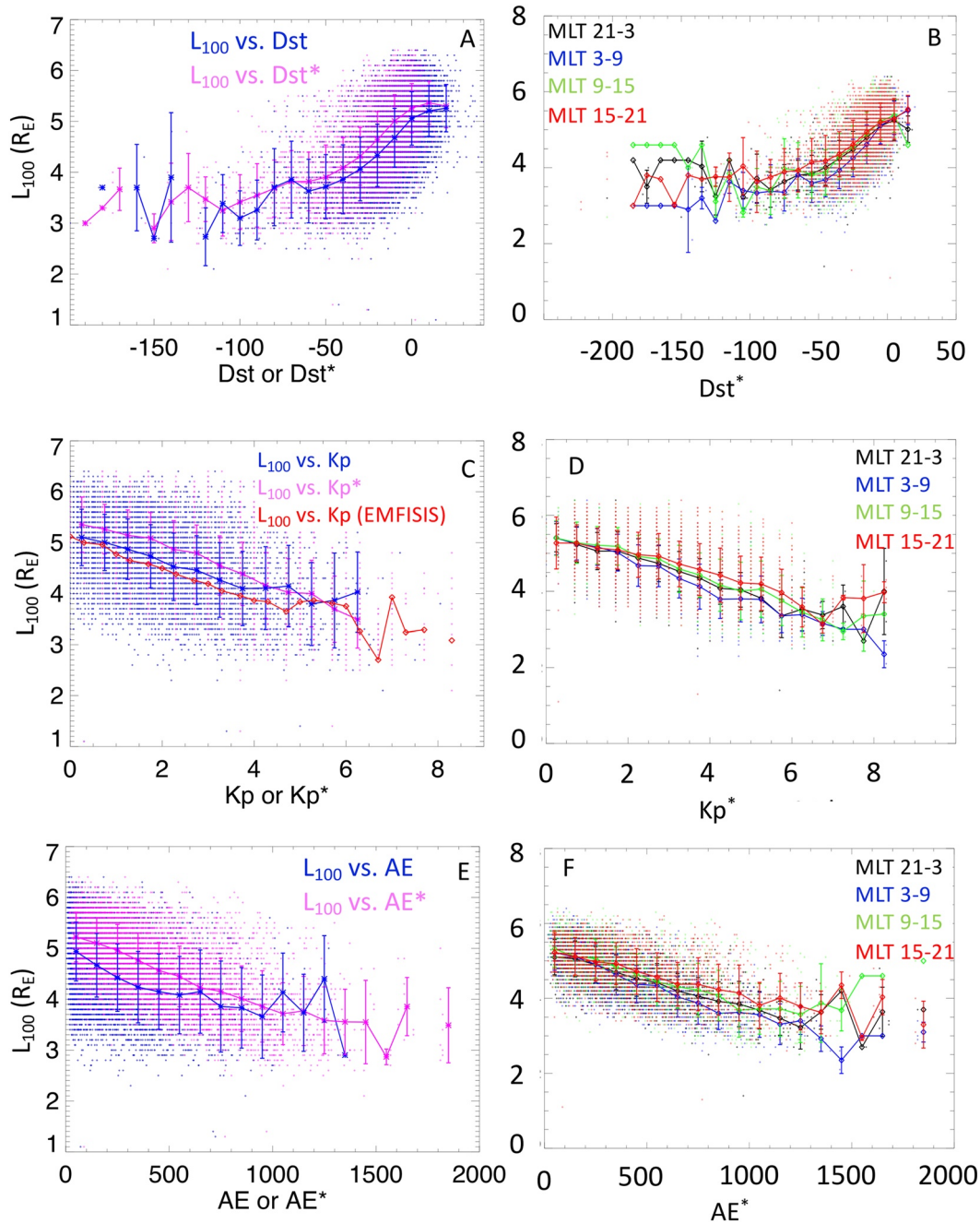

Figure 3. Empirical models of the 100 cm^{-3} plasmasphere outer edge (left) averaged over magnetic local time (MLT) and (right) for 4 MLT sectors as a function of geomagnetic activity; (top) Dst and Dst*, (center) Kp and Kp*, and (bottom) AE and AE* with (dots) all values, (blue or pink lines) the Electric Field and Waves mean, (red line) the Electric and Magnetic Field Instrument Suite and Integrated Science mean, and the standard deviation (bars).

of the difference (normalized in % of data), $D = (L_{100} - L_{\text{model or CA92}})$ shows the new model is centered at $D \sim 0$ L while CA92 is indeed shifted by ~+0.1 L (Figure 4e) for all Kp. For individual increasing Kp*, the shift in difference increases toward larger positive differences (Figures 4f and 4g). Wider difference bins of *good* ($|D| \leq 0.1$ L) and *poor* ($|D| \geq 0.1$ L) accuracy shows the increasing difference of CA92 from the L_{100} data as Kp* increases, while the new model stays more centered around $D = 0$L (Figure 4h).

The normalized difference (ND) spread is plotted versus the L_{100} data and is lower for the new model (Figure 4i) compared with CA92 in Figure 4j. The CA92 difference is positive in 72% of the cases with difference increasing

19448007, 2022, 21, Downloaded from https://agupubs.onlinelibrary.wiley.com/doi/10.1029/2022GL101402 by EVIDENCE AID - BELGIUM, Wiley Online Library on [05/11/2022]. See the Terms and Conditions (https://onlinelibrary.wiley.com/terms-and-conditions) on Wiley Online Library for rules of use; OA articles are governed by the applicable Creative Commons License

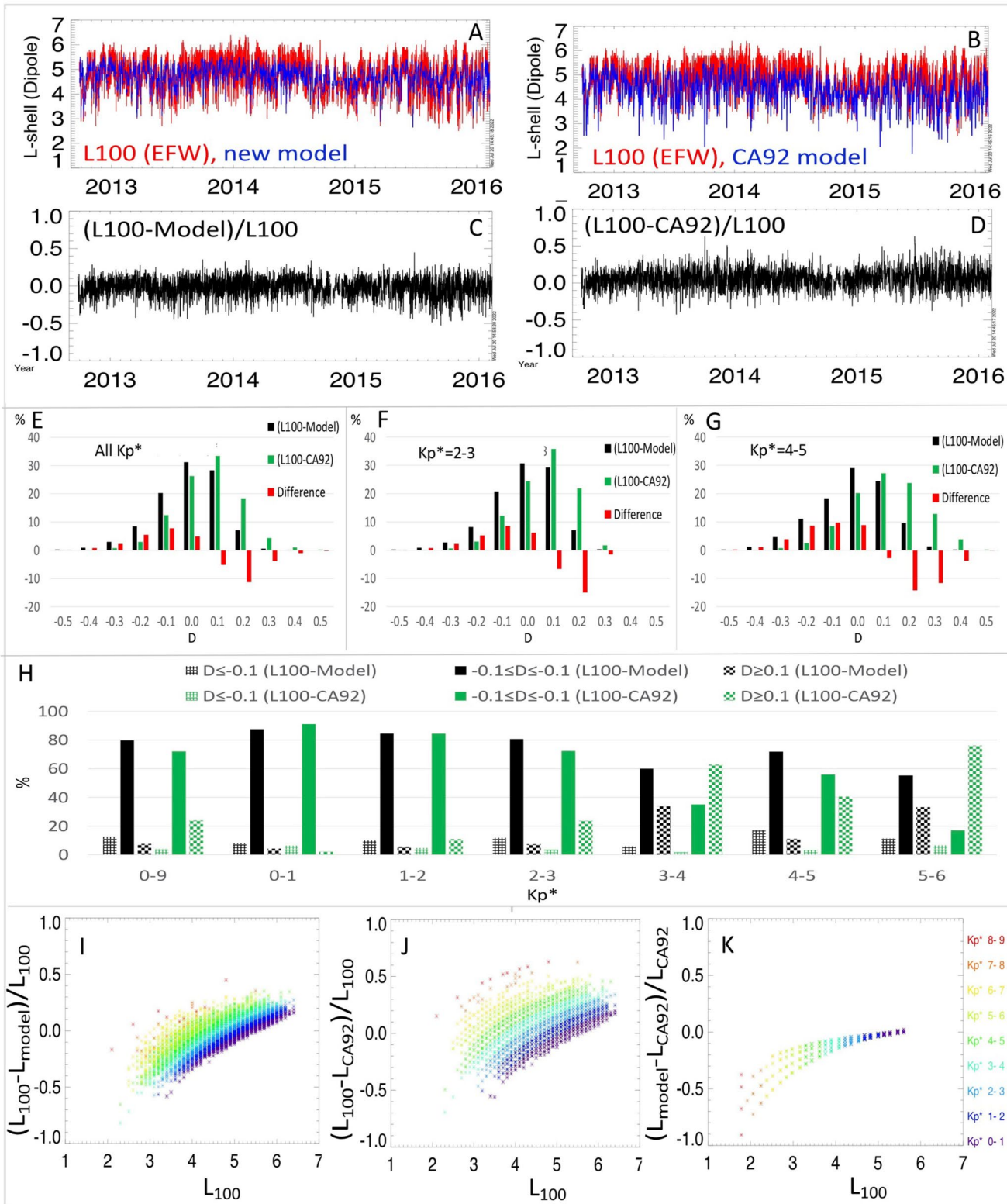

Figure 4. (a) Kp*-magnetic local time-dependent model of Section 4 and (b) CA92 model are compared with L_{100} (Electric Field and Waves) data, with (c and d) their respective normalized difference. The distribution (in %) of the difference D (in L) for (e) all and (f and g) some Kp* bins. (h) Distribution reduced to three large bins of D (in L) versus Kp* bins. Normalized difference spread versus L_{100} colored by Kp* for (i) this and (j) CA92 models and (k) their difference.

19448007, 2022, 21, Downloaded from https://agupubs.onlinelibrary.wiley.com/doi/10.1029/2022GL101402 by EVIDENCE AID - BELGIUM, Wiley Online Library on [05/11/2022]. See the Terms and Conditions (https://onlinelibrary.wiley.com/terms-and-conditions) on Wiley Online Library for rules of use; OA articles are governed by the applicable Creative Commons License

with L-shell and Kp* increasing, up to ND ∼ +0.6 (Figure 4j). Conversely, the CA92 difference is negative for 28% of the cases, with larger differences at small Kp*. Computing the normalized difference between both models in Figure 4k shows the new model performs similarly to CA92 at low Kp* and high L (due to comparable b values). However, they depart from each other with L decreasing and Kp* increasing, with the new model closer to the L_{100} observations. We suggest the high b value of CA92 (also found for the gradient applied to EMFISIS data) can come from gradients occurring in the very low density fluctuating regions (ne ∼ <10–30 cm^{-3}) as ∼0.9% of L_{100} versus 9% L_{pp} are found for $n_e \leq 30$ cm^{-3} in Figure 2c (EMFISIS data). This can statistically push the L_{pp} to higher L and could compensate the lack of dusk side statistics (15–24 MLT) in the CA92 model.

Differences can be caused by the absence of MLT dependence in CA92 and the general bias of the gradient method of CA92 for the night side and active times (cf. Section 3). Geomagnetic conditions are also different since Van Allen Probes data were collected under relatively quiet conditions. Finally, the large density variability (some due to the MLT-dependence above Kp* ∼ 2) causes regular departure from any mean model.

6. Summary and Conclusions

We statistically study the Earth's plasmasphere boundaries through the plasmapause location defined by a gradient at L_{pp} and the 100 cm^{-3} threshold for the plasmasphere dense outer edge at L_{100} using both EFW spacecraft floating potential and EMFISIS f_{UHR} cold electron plasma densities.

Direct comparison of L_{100} and L_{pp} when both are defined shows 53% of differences are within [−0.1 L, 0.1 L], 69% within [−0.2 L, 0.2 L], 77% within [−0.3 L, 0.3 L], and 86% within [−0.5 L, 0.5 L]. The density difference at L_{100} and L_{pp} is ±100 cm^{-3} for 75% of cases. Normalized by L_{pp}, a difference of (±50%, ±100%, ±200%) represents (37%, 82%, 93%) of cases. Thus, the L_{100} location encompasses (or approximates) the plasmapause when a gradient exists. When a gradient is not defined (47% of cases), L_{100} reliably provides an L-shell limit (∼85% of cases). This is particularly evident in the dusk region and for an extended plasmasphere, where L_{100} is more readily determined than L_{pp}, therefore avoiding a statistical bias on the night/dawn side, and permits the reliable separation between hiss and chorus in radiation belt models. These results confirm *Carpenter's knee* occurs in the vicinity of ∼100 cm^{-3}, and supports a labeling of the outer edge of the plasmasphere at ∼100 cm^{-3} as the plasmapause.

Daily observations show a great expansion of the plasmasphere, with L_{100} data reaching $L = 5.5 \pm 0.25$ commonly (18% of data) and up to $L = 6 \pm 0.25$ (5%), which confirms the influence of the plasmasphere (through the hiss power contained within) far inside the outer radiation belt.

The L_{100} location becomes MLT-dependent for Dst* < −20, AE* > 600, and Kp* > 3, which justifies keeping the MLT dependence in the new models. The L_{100} standard deviation varies from ∼±0.5 L for quiet times (Kp < 2, AE < 300, and Dst > −50) up to ∼±1 L for active times. The width of the plasmasphere edge is generally small (sharp gradient) on the night side for non-quiet times and a wide boundary layer in the afternoon sector for any Kp.

Statistics are used to create a new generation of empirical plasmapause models with respect to L-shell, MLT, and geomagnetic indices, with a mean value and a standard deviation for uncertainty quantification. They are made to better organize the whistler-mode waves inside and outside of the plasmasphere, drastically influencing the accuracy of now- and forecasting of space weather codes.

New linear dependences $L_{100/pp} = b - a\mathrm{Kp}^*$ have been generated. Using EMFISIS data and the gradient method, we recover the Carpenter and Anderson (1992) L_{pp} model (CA92), showing the practical reliability of this model. However, direct comparisons of the new L_{100} fits, the CA92 model, and L_{100} observations show the dense plasmasphere expands farther out than what predicted from the CA92 model. Departure of the CA92 model from the L_{100} data increases as Kp* increases and L-shell decreases, while the new fits perform better. Storm-induced erosions are not as deep as predicted by the CA92 model. Consequently, past radiation belt simulations using the CA92 model can have chorus waves misplaced too deep in L-shell, possibly overestimating local acceleration and underestimating electron scattering by hiss waves.

Future parametrization of the Earth's plasmasphere boundaries should cumulate more indices and their history to better reproduce the large variability observed within a single fixed index bin, which will be reachable using machine learning techniques.

19448007, 2022, 21, Downloaded from https://agupubs.onlinelibrary.wiley.com/doi/10.1029/2022GL101402 by EVIDENCE AID - BELGIUM, Wiley Online Library on [05/11/2022]. See the Terms and Conditions (https://onlinelibrary.wiley.com/terms-and-conditions) on Wiley Online Library for rules of use; OA articles are governed by the applicable Creative Commons License

Data Availability Statement

Van Allen Probes A EMFISIS data are available at https://doi.org/10.48322/c4ha-xj50. Van Allen Probes B EMFISIS data are available at https://doi.org/10.48322/c6s1-wg66. Van Allen Probes wave data used in this work are also available from the EFW and EMFISIS team websites (which one can find at http://rbspgway.jhuapl.edu). The plasmapause empirical models (made of the mean and standard deviation of all panels of Figure 4) are provided through text files which can be downloaded in the link of Thaller and Ripoll (2022). Figures and files for Figure 3 (left) with respect to non-starred indices are also provided for Van Allen Probes B as well as statistics and laws generated from Van Allen Probes A measurements (October 2012–April 2016) (Thaller & Ripoll, 2022).

Acknowledgments
The authors thank the EFW and EMFISIS teams of the Van Allen Probes mission for their support. The authors thank the National Science Foundation Geospace Environment Modeling Project 2040708. The authors thank the International Space Sciences Institute (ISSI) and the participants in a 2020 ISSI workshop for the project "Radiation belts physics." The work of J.-F.R. and G.S.C. was performed under the auspices of an agreement between Commissariat à l'Energie Atomique, Direction des Applications Militaires (CEA/DAM) and National Nuclear Security Administration, Defense Program (NNSA/DP) on cooperation on fundamental science. D.P.H. acknowledges NASA Grant 80NSSC20K1324. V.P. acknowledges the Horizon 2020 PITHIA-NRF grant agreement No. 101007599.

References

Albert, J. M. (2005). Evaluation of quasi-linear diffusion coefficients for whistler mode waves in a plasma with arbitrary density ratio. *Journal of Geophysical Research*, *110*(A3), A03218. https://doi.org/10.1029/2004JA010844

Bandić, M., Verbanac, G., Moldwin, M. B., Pierrard, V., & Piredda, G. (2016). MLT dependence in the relationship between plasmapause, solar wind, and geomagnetic activity based on CRRES: 1990–1991. *Journal of Geophysical Research: Space Physics*, *121*(5), 4397–4408. https://doi.org/10.1002/2015JA022278

Borovsky, J. E., & Denton, M. H. (2008). A statistical look at plasmaspheric drainage plumes. *Journal of Geophysical Research*, *113*(A9), A09221. https://doi.org/10.1029/2007JA012994

Botek, E., Pierrard, V., & Darrouzet, F. (2021). Assessment of the Earth's cold plasmatrough modeling by using Van Allen Probes/EMFISIS and Arase/PWE electron density data. *Journal of Geophysical Research: Space Physics*, *126*(12), e2021JA029737. https://doi.org/10.1029/2021JA029737

Camporeale, E., Shprits, Y., Chandorkar, M., Drozdov, A., & Wing, S. (2016). On the propagation of uncertainties in radiation belt simulations. *Space Weather*, *14*(11), 982–992. https://doi.org/10.1002/2016SW001494

Carpenter, D. L. (1966). Whistler studies of the plasmapause in the magnetosphere: 1. Temporal variations in the position of the knee and some evidence on plasma motions near the knee. *Journal of Geophysical Research*, *71*(3), 693–709. https://doi.org/10.1029/jz071i003p00693

Carpenter, D. L., & Anderson, R. R. (1992). An ISEE/whistler model of equatorial electron density in the magnetosphere. *Journal of Geophysical Research*, *97*(A2), 1097–1108. https://doi.org/10.1029/91JA01548

Carpenter, D. L., Anderson, R. R., Calvert, W., & Moldwin, M. B. (2000). CRRES observations of density cavities inside the plasmasphere. *Journal of Geophysical Research*, *105*(A10), 23323–23338. https://doi.org/10.1029/2000JA000013

Carpenter, D. L., & Lemaire, J. (2004). The plasmasphere boundary layer. *Annales Geophysicae*, *22*(12), 4291–4298. https://doi.org/10.5194/angeo-22-4291-2004

Cervantes, S., Shprits, Y. Y., Aseev, N. A., & Allison, H. J. (2020). Quantifying the effects of EMIC wave scattering and magnetopause shadowing in the outer electron radiation belt by means of data assimilation. *Journal of Geophysical Research: Space Physics*, *125*(8), e2020JA028208. https://doi.org/10.1029/2020JA028208

Cervantes, S., Shprits, Y. Y., Aseev, N. A., Drozdov, A. Y., Castillo, A., & Stolle, C. (2020). Identifying radiation belt electron source and loss processes by assimilating spacecraft data in a three-dimensional diffusion model. *Journal of Geophysical Research: Space Physics*, *125*(1), e2019JA027514. https://doi.org/10.1029/2019JA027514

Cho, J., Lee, D.-Y., Kim, J.-H., Shin, D.-K., Kim, K.-C., & Turner, D. (2015). New model fit functions of the plasmapause location determined using THEMIS observations during the ascending phase of solar cycle 24. *Journal of Geophysical Research: Space Physics*, *120*(4), 2877–2889. https://doi.org/10.1002/2015JA021030

Denton, R. E., Menietti, J. D., Goldstein, J., Young, S. L., & Anderson, R. R. (2004). Electron density in the magnetosphere. *Journal of Geophysical Research*, *109*(A9), A09215. https://doi.org/10.1029/2003JA010245

Escoubet, C. P., Pedersen, A., Schmidt, R., & Lindqvist, P. A. (1997). Density in the magnetosphere inferred from ISEE 1 spacecraft potential. *Journal of Geophysical Research*, *102*(A8), 17595–17609. https://doi.org/10.1029/97JA00290

Glauert, S. A., Horne, R. B., & Meredith, N. P. (2014). Three-dimensional electron radiation belt simulations using the BAS Radiation Belt Model with new diffusion models for chorus, plasmaspheric hiss, and lightning-generated whistlers. *Journal of Geophysical Research: Space Physics*, *119*(1), 268–289. https://doi.org/10.1002/2013JA019281

Glauert, S. A., Horne, R. B., & Meredith, N. P. (2018). A 30-year simulation of the outer electron radiation belt. *Space Weather*, *16*(10), 1498–1522. https://doi.org/10.1029/2018SW001981

Goldstein, J., Pascuale, S., & Kurth, W. S. (2019). Epoch-based model for stormtime plasmapause location. *Journal of Geophysical Research: Space Physics*, *124*(6), 4462–4491. https://doi.org/10.1029/2018JA025996

Goldstein, J., Sandel, B. R., Forrester, W. T., & Reiff, P. H. (2003). IMF-driven plasmasphere erosion of 10 July 2000. *Geophysical Research Letters*, *30*(3), 1146. https://doi.org/10.1029/2002GL016478

Goldstein, J., Spasojević, M., Reiff, P. H., Sandel, B. R., Forrester, W. T., Gallagher, D. L., & Reinisch, B. W. (2003). Identifying the plasmapause in IMAGE EUV data using IMAGE RPI in situ steep density gradients. *Journal of Geophysical Research*, *108*(A4), 1147. https://doi.org/10.1029/2002JA009475

Guo, D., Fu, S., Xiang, Z., Ni, B., Guo, Y., Feng, M., et al. (2021). Prediction of dynamic plasmapause location using a neural network. *Space Weather*, *19*, e2020SW002622. https://doi.org/10.1029/2020SW002622

He, F., Zhang, X.-X., Lin, R.-L., Fok, M.-C., Katus, R. M., Liemohn, M. W., et al. (2017). A new solar wind-driven global dynamic plasmapause model: 2. Model and validation. *Journal of Geophysical Research: Space Physics*, *122*(7), 7172–7187. https://doi.org/10.1002/2017JA023913

Jahn, J., Goldstein, J., Kurth, W., Thaller, S., De Pascuale, S., Wygant, J., et al. (2020). Determining plasmaspheric density from the upper hybrid resonance and from spacecraft potential: How do they compare? *Journal of Geophysical Research: Space Physics*, *125*, 1–17. https://doi.org/10.1029/2019JA026860

Kim, K.-C., Shprits, Y., Subbotin, D., & Ni, B. (2011). Understanding the dynamic evolution of the relativistic electron slot region including radial and pitch angle diffusion. *Journal of Geophysical Research*, *116*(A10), A10214. https://doi.org/10.1029/2011JA016684

Kletzing, C. A., Kurth, W. S., Acuna, M., MacDowall, R. J., Torbert, R. B., Averkamp, T., et al. (2013). The electric and magnetic field instrument suite and integrated science (EMFISIS) on RBSP. *Space Science Reviews*, *179*(1–4), 127–181. https://doi.org/10.1007/s11214-013-9993-6

19448007, 2022, 21, Downloaded from https://agupubs.onlinelibrary.wiley.com/doi/10.1029/2022GL101402 by EVIDENCE AID - BELGIUM, Wiley Online Library on [05/11/2022]. See the Terms and Conditions (https://onlinelibrary.wiley.com/terms-and-conditions) on Wiley Online Library for rules of use; OA articles are governed by the applicable Creative Commons License

Krall, J., Huba, J. D., & Borovsky, J. E. (2018). SAMI3 simulations of a persistent plasmasphere plume. *Geophysical Research Letters*, *45*(8), 3374–3381. https://doi.org/10.1002/2017GL076448

Kurth, W. S., De Pascuale, S., Faden, J. B., Kletzing, C. A., Hospodarsky, G. B., Thaller, S., & Wygant, J. R. (2015). Electron densities inferred from plasma wave spectra obtained by the waves instrument on Van Allen Probes. *Journal of Geophysical Research: Space Physics*, *120*(2), 904–914. https://doi.org/10.1002/2014JA020857

Larsen, B. A., Klumpar, D. M., & Gurgiolo, C. (2007). Correlation between plasmapause position and solar wind parameters. *Journal of Atmospheric and Solar-Terrestrial Physics*, *69*(3), 334–340. https://doi.org/10.1016/j.jastp.2006.06.017

Li, W., Ni, B., Thorne, R. M., Bortnik, J., Nishimura, Y., Green, J. C., et al. (2014). Quantifying hiss-driven energetic electron precipitation: A detailed conjunction event analysis. *Geophysical Research Letters*, *41*(4), 1085–1092. https://doi.org/10.1002/2013GL059132

Liu, X., Liu, W., Cao, J. B., Fu, H. S., Yu, J., & Li, X. (2015). Dynamic plasmapause model based on THEMIS measurements. *Journal of Geophysical Research: Space Physics*, *120*(12), 10543–10556. https://doi.org/10.1002/2015JA021801

Liu, X., & Liu, W.-L. (2014). A new plasmapause location model based on THEMIS observations. *Science China Earth Sciences*, *57*(10), 2552–2557. https://doi.org/10.1007/s11430-014-4844-1

Malaspina, D. M., Jaynes, A. N., Boulé, C., Bortnik, J., Thaller, S. A., Ergun, R. E., et al. (2016). The distribution of plasmaspheric hiss wave power with respect to plasmapause location. *Geophysical Review Letters*, *43*(15), 7878–7886. https://doi.org/10.1002/2016GL069982

Malaspina, D. M., Jaynes, A. N., Elkington, S., Chan, A., Hospodarsky, G., & Wygant, J. (2021). Testing the organization of lower-band whistler-mode chorus wave properties by plasmapause location. *Journal of Geophysical Research: Space Physics*, *126*(1), e2020JA028458. https://doi.org/10.1029/2020JA028458

Malaspina, D. M., Ripoll, J.-F., Chu, X., Hospodarsky, G., & Wygant, J. (2018). Variation in plasmaspheric hiss wave power with plasma density. *Geophysical Research Letters*, *45*(18), 9417–9426. https://doi.org/10.1029/2018GL078564

Malaspina, D. M., Zhu, H., & Drozdov, A. Y. (2020). A wave model and diffusion coefficients for plasmaspheric hiss parameterized by plasmapause location. *Journal of Geophysical Research: Space Physics*, *125*(2), e2019JA027415. https://doi.org/10.1029/2019JA027415

Mauk, B. H., Fox, N. J., Kanekal, S. G., Kessel, R. L., Sibeck, D. G., & Ukhorskiy, A. (2013). Science objectives and rationale for the radiation belt storm probes mission. *Space Science Reviews*, *179*(1–4), 3–27. https://doi.org/10.1007/s11214-012-9908-y

Millan, R. M., Ripoll, J.-F., Santolík, O., & Kurth, W. S. (2021). Early-time non-equilibrium pitch angle diffusion of electrons by whistler-mode hiss in a plasmaspheric plume associated with BARREL precipitation. *Frontiers in Astronomy and Space Science*, *8*, 776992. https://doi.org/10.3389/fspas.2021.776992

Moldwin, M. B., Downward, L., Rassoul, H. K., Amin, R., & An- derson, R. R. (2002). A new model of the location of the plasmapause: CRRES results. *Journal of Geophysical Research*, *107*(A11), 1339. https://doi.org/10.1029/2001JA009211

O'Brien, T. P., & Moldwin, M. B. (2003). Empirical plasmapause models from magnetic indices. *Geophysical Research Letters*, *30*(4), 1152. https://doi.org/10.1029/2002GL016007

Ozeke, L. G., Mann, I. R., Claudepierre, S. G., Henderson, M., Morley, S. K., Murphy, K. R., et al. (2019). The March 2015 superstorm revisited: Phase space density profiles and fast ULF wave diffusive transport. *Journal of Geophysical Research: Space Physics*, *124*(2), 1143–1156. https://doi.org/10.1029/2018JA026326

Pierrard, V., Botek, E., & Darrouzet, F. (2021). Improving predictions of the 3D dynamic model of the plasmasphere. *Frontiers in Astronomy and Space Sciences*, *8*, 681401. https://doi.org/10.3389/fspas.2021.681401

Pierrard, V., Botek, E., Ripoll, J.-F., Thaller, S. A., Moldwin, M. B., Ruohoniemi, M., & Reeves, G. (2021). Links of the plasmapause with other boundary layers of the magnetosphere: Ionospheric convection, radiation belt boundaries. Auroral Oval. *Frontiers in Astronomy and Space Sciences*, *8*, 728531. https://doi.org/10.3389/fspas.2021.728531

Pierrard, V., Ripoll, J.-F., Cunningham, G., Botek, E., Santolik, O., Thaller, S., et al. (2021). Observations and simulations of dropout events and flux decays in October 2013: Comparing MEO equatorial with LEO polar orbit. *Journal of Geophysical Research: Space Physics*, *126*(6), e2020JA028850. https://doi.org/10.1029/2020JA028850

Pierrard, V., & Rosson, L. G. (2016). The effects of the big storm events in the first half of 2015 on the radiation belts observed by EPT/PROBA-V. *Annales Geophysicae*, *34*(1), 75–84. https://doi.org/10.5194/angeo-34-75-2016

Reidy, J. A., Horne, R. B., Glauert, S. A., Clilverd, M. A., Meredith, N. P., Woodfield, E. E., et al. (2021). Comparing electron precipitation fluxes calculated from pitch angle diffusion coefficients to LEO satellite observations. *Journal of Geophysical Research: Space Physics*, *126*(3), e2020JA028410. https://doi.org/10.1029/2020JA028410

Ripoll, J.-F., Claudepierre, S. G., Ukhorskiy, A. Y., Colpitts, C., Li, X., Fennell, J., & Crabtree, C. (2020). Particle dynamics in the Earth's radiation belts: Review of current research and open questions. *Journal of Geophysical Research: Space Physics*, *125*(5), e2019JA026735. https://doi.org/10.1029/2019JA026735

Ripoll, J.-F., Denton, M., Loridan, V., Santolík, O., Malaspina, D., Hartley, D. P., et al. (2020). How whistler mode hiss waves and the plasmasphere drive the quiet decay of radiation belts electrons following a geomagnetic storm. *Journal of Physics: Conference Series*, *1623*, 012005. https://doi.org/10.1088/1742-6596/1623/1/012005

Ripoll, J.-F., Denton, M. H., Hartley, D. P., Reeves, G. D., Malaspina, D., Cunningham, G. S., et al. (2020). Scattering by whistler-mode waves during a quiet period perturbed by substorm activity. *Journal of Atmospheric and Solar-Terrestrial Physics*, *215*, 105471. https://doi.org/10.1016/j.jastp.2020.105471

Ripoll, J.-F., Loridan, V., Denton, M. H., Cunningham, G., Reeves, G., Santolík, O., et al. (2019). Observations and Fokker-Planck simulations of the *L*-shell, energy, and pitch angle structure of Earth's electron radiation belts during quiet times. *Journal of Geophysical Research: Space Physics*, *124*(2), 1125–1142. https://doi.org/10.1029/2018ja026111

Ripoll, J.-F., Reeves, G. D., Cunningham, G. S., Loridan, V., Denton, M., Santolik, O., et al. (2016). Reproducing the observed energy dependent structure of Earth's electron radiation belts during storm recovery with an event-specific diffusion model. *Geophysical Research Letters*, *43*(11), 5616–5625. https://doi.org/10.1002/2016GL068869

Ripoll, J.-F., Santolík, O., Reeves, G. D., Kurth, W. S., Denton, M. H., Loridan, V., et al. (2017). Effects of whistler mode hiss waves in March 2013. *Journal of Geophysical Research: Space Physics*, *122*(7), 7433–7462. https://doi.org/10.1002/2017JA024139

Saikin, A. A., Shprits, Y. Y., Drozdov, A. Y., Landis, D. A., Zhelavskaya, I. S., & Cervantes, S. (2021). Reconstruction of the radiation belts for solar cycles 17–24 (1933–2017). *Space Weather*, *19*(3), e2020SW002524. https://doi.org/10.1029/2020SW002524

Shprits, Y., Subbotin, D., Drozdov, A., Usanova, M. E., Kellerman, A., Orlova, K., et al. (2013). Unusual stable trapping of the ultrarelativistic electrons in the Van Allen radiation belts. *Nature Physics*, *9*(11), 699–703. https://doi.org/10.1038/nphys2760

Subbotin, D. A., & Shprits, Y. Y. (2009). Three-dimensional modeling of the radiation belts using the Versatile Electron Radiation Belt (VERB) code. *Space Weather*, *7*(10), S10001. https://doi.org/10.1029/2008SW000452

Thaller, S. A., & Ripoll, J.-F. (2022). Plasmapause location empirical laws from spacecraft charging of the Van Allen Probes [Dataset]. Zenodo. https://doi.org/10.5281/zenodo.5889253

19448007, 2022, 21, Downloaded from https://agupubs.onlinelibrary.wiley.com/doi/10.1029/2022GL101402 by EVIDENCE AID - BELGIUM, Wiley Online Library on [05/11/2022]. See the Terms and Conditions (https://onlinelibrary.wiley.com/terms-and-conditions) on Wiley Online Library for rules of use; OA articles are governed by the applicable Creative Commons License

Thaller, S. A., Wygant, J. R., Dai, L., Breneman, A. W., Kersten, K., Cattell, C. A., et al. (2015). Van allen Probes investigation of the large-scale duskward electric field and its role in ring current formation and plasmasphere erosion in the 1 June 2013 storm. *Journal of Geophysical Research: Space Physics*, *120*(6), 4531–4543. https://doi.org/10.1002/2014ja020875

Thorne, R. M. (2010). Radiation belt dynamics: The importance of wave-particle interactions. *Geophysical Research Letters*, *37*(22), L22107. https://doi.org/10.1029/2010GL044990

Torkar, K., Nakamura, R., Tajmar, M., Scharlemann, C., Jeszenszky, H., Laky, G., et al. (2016). Active spacecraft potential control investigation. *Space Science Reviews*, *199*(1–4), 515–544. https://doi.org/10.1007/s11214-014-0049-3

Torkar, K., Nakamura, R., Wellenzohn, S., Jeszenszky, H., Torbert, R. B., Lindqvist, P. A., et al. (2019). Improved determination of plasma density based on spacecraft potential of the magnetospheric multiscale mission under active potential control. *IEEE Transactions on Plasma Science*, *47*(8), 3636–3647. https://doi.org/10.1109/TPS.2019.2911425

Tu, J., Song, P., Reinisch, B. W., & Green, J. L. (2007). Smooth electron density transition from plasmasphere to the subauroral region. *Journal of Geophysical Research*, *112*(A5), A05227. https://doi.org/10.1029/2007JA012298

Tu, W., Cunningham, G. S., Chen, Y., Henderson, M. G., Camporeale, E., & Reeves, G. D. (2013). Modeling radiation belt electron dynamics during GEM challenge intervals with the DREAM3D diffusion model. *Journal of Geophysical Research: Space Physics*, *118*(10), 6197–6211. https://doi.org/10.1002/jgra.50560

Tu, W., Li, X., Chen, Y., Reeves, G. D., & Temerin, M. (2009). Storm-dependent radiation belt electron dynamics. *Journal of Geophysical Research*, *114*(A2), A02217. https://doi.org/10.1029/2008JA013480

Verbanac, G., Pierrard, V., Bandić, M., Darrouzet, F., Rauch, J.-L., & Décréau, P. (2015). The relationship between plasmapause, solar wind and geomagnetic activity between 2007 and 2011. *Annales Geophysicae*, *33*(10), 1271–1283. https://doi.org/10.5194/angeo-33-1271-2015

Wang, D., & Shprits, Y. Y. (2019). On how high-latitude chorus waves tip the balance between acceleration and loss of relativistic electrons. *Geophysical Research Letters*, *46*(14), 7945–7954. https://doi.org/10.1029/2019GL082681

Wygant, J. R., Bonnell, J. W., Goetz, K., Ergun, R. E., Mozer, F. S., Bale, S. D., et al. (2013). The electric field and waves instruments on the radiation belt storm Probes mission. *Space Science Reviews*, *179*(1-4), 183–220. https://doi.org/10.1007/s11214-013-0013-7

Zhao, H., Ni, B., Li, X., Baker, D. N., Johnston, W. R., Zhang, W., et al. (2019). Plasmaspheric hiss waves generate a reversed energy spectrum of radiation belt electrons. *Nature Physics*, *15*(4), 367–372. https://doi.org/10.1038/s41567-018-0391-6

19448007, 2022, 21, Downloaded from https://agupubs.onlinelibrary.wiley.com/doi/10.1029/2022GL101402 by EVIDENCE AID - BELGIUM, Wiley Online Library on [05/11/2022]. See the Terms and Conditions (https://onlinelibrary.wiley.com/terms-and-conditions) on Wiley Online Library for rules of use; OA articles are governed by the applicable Creative Commons License